

JGR Atmospheres

RESEARCH ARTICLE

10.1029/2023JD039667

Key Points:

- Raindrop size distributions simulated using a bin microphysics scheme are evaluated in comparison with disdrometer observations
- For stratiform rain, the number of large raindrops is overestimated due to overgrowth of snow particles by aggregation and their melting
- When convective rain is largely involved, the number of small raindrops is overestimated due to insufficient warm-rain collision–coalescence

Correspondence to:

J.-J. Baik and H.-G. Jin,
jjbaik@snu.ac.kr;
hgjin@pusan.ac.kr

Citation:

Lee, J., Baik, J.-J., & Jin, H.-G. (2024). Raindrop size distributions simulated using a bin microphysics scheme: Different biases in stratiform and convective rain from an extratropical cyclone. *Journal of Geophysical Research: Atmospheres*, 129, e2023JD039667. <https://doi.org/10.1029/2023JD039667>

Received 17 JULY 2023

Accepted 5 MAR 2024

Raindrop Size Distributions Simulated Using a Bin Microphysics Scheme: Different Biases in Stratiform and Convective Rain From an Extratropical Cyclone

Joohyun Lee¹ , Jong-Jin Baik¹ , and Han-Gyul Jin² 

¹School of Earth and Environmental Sciences, Seoul National University, Seoul, South Korea, ²Department of Atmospheric Sciences, Pusan National University, Busan, South Korea

Abstract Bin microphysics schemes prognose the raindrop size distribution (RSD), which can be directly evaluated through comparison with disdrometer observations. This evaluation will provide implications on the reliability of simulated cloud microphysics by bin microphysics schemes. In this study, the RSDs of a precipitation event associated with an extratropical cyclone passing South Korea are simulated using a bin microphysics scheme and compared with those observed by a ground-based disdrometer. The simulated mean RSD overall agrees with the observation. However, notable overestimations appear in the large- (3.3–4.3 mm) and small- (0.56–1.88 mm) diameter ranges, which respectively stem from the biases in two different time periods, one dominated by stratiform rain and the other largely involved with convective rain. In the stratiform-rain-dominated period, the melting of snow is the largest contributor to RSDs. The overestimation in the large-diameter range in this period can be associated with overly active ice–ice collection at upper levels, which generates a local maximum in RSD at the diameter of 3.3 mm that is not seen in the observed RSDs. In the convective-rain-involved period, the warm-rain collision–coalescence is the largest contributor to RSDs. The overestimation in the small-diameter range and underestimation in the large-diameter range imply that the collisional growth of raindrops is represented to be weaker than that in reality. The findings in this study suggest that the RSDs simulated using a bin microphysics scheme can have some systematic biases associated with misrepresentation of some microphysical processes.

Plain Language Summary Bin microphysics schemes are a type of cloud microphysics schemes that allow for the particle size distributions of hydrometeors to take any form at the expense of huge computational resources, aiming to represent the cloud microphysics as realistically as possible. In this study, the raindrop size distributions predicted using a bin microphysics scheme are evaluated through comparison with ground-based observations obtained using a disdrometer. The mean raindrop size distribution is overall well reproduced, but the raindrop number concentration is overestimated in the small- and large-diameter ranges. The overestimation in the large-diameter range occurs in the period when stratiform rain is dominant, attributable to the overgrowth of ice particles via ice–ice collection and their melting into large raindrops. The overestimation in the small-diameter range occurs in the period when convective rain is largely involved, which is attributed to the insufficient growth of raindrops via coalescence with other drops.

1. Introduction

In cloud-resolving models, the cloud microphysical processes are represented using either bulk or bin microphysics schemes. The main difference between the two types of schemes is how the size distribution of hydrometeors is treated. While bulk microphysics schemes assume the size distribution of any hydrometeor to follow a specific distribution (e.g., exponential, gamma, and log-normal distribution), bin microphysics schemes explicitly predict the size distribution of any hydrometeor using size (mass) bins. The explicit prediction of hydrometeor size distributions by bin microphysics schemes enables to numerically solve the governing equations for microphysical processes with minimal approximations. This approach generally leads to improved prediction performance compared to bulk microphysics schemes (Iguchi, Nakajima, et al., 2012; Lee & Baik, 2018; Lynn & Khain, 2007), despite some inherent issues (Grabowski et al., 2019; Morrison et al., 2018).

Hydrometeor size distributions predicted using a bin microphysics scheme can be directly compared with observed distributions, which provides a more informative evaluation of precipitation simulations than comparing bulk precipitation characteristics such as precipitation rate. Hydrometeor size distributions contain information

© 2024. The Authors.

This is an open access article under the terms of the [Creative Commons Attribution-NonCommercial-NoDerivs License](#), which permits use and distribution in any medium, provided the original work is properly cited, the use is non-commercial and no modifications or adaptations are made.

about the dominant microphysical processes involved in the clouds (Rosenfeld & Ulbrich, 2003). For example, the collision–coalescence between raindrops decreases the number concentration of small raindrops and increases that of large raindrops, while the breakup of raindrops acts in the opposite manner. Therefore, the evaluation of simulated hydrometeor size distributions provides an indirect evaluation of simulated cloud microphysics, which is valuable because directly evaluating the microphysical process rates in the simulation based on in-situ observations is extremely difficult.

There have been some studies that evaluated the hydrometeor size distributions simulated using bin microphysics schemes (Chen et al., 2023; Fridlind et al., 2017; Hernández Pardo et al., 2021; Iguchi, Matsui, et al., 2012; Khairoutdinov & Kogan, 1999; Morrison et al., 2022; Shpund et al., 2019; Witte et al., 2019). Khairoutdinov and Kogan (1999) and Witte et al. (2019) evaluated the simulated cloud drop size distributions in marine stratocumulus in comparison with aircraft observations and both found prominent discrepancies at the cloud boundaries. The discrepancies were attributed to the inaccurate representation of small-scale entrainment and mixing due to insufficient spatial resolution (Khairoutdinov & Kogan, 1999) and to a spurious peak of supersaturation generated by numerical problems (Witte et al., 2019). Shpund et al. (2019) simulated a rainfall event during Midlatitude Continental Convective Cloud Experiment (MC3E) and showed that the snow particle number concentration decreases with decreasing height in a larger rate in the simulation than in the aircraft observations. They suggested that the lack of ice fragmentation by collision between ice particles in the simulation is one of the possible reasons.

The evaluation of raindrop size distribution (RSD) has been performed using ground-based disdrometers (Chen et al., 2023; Iguchi, Matsui, et al., 2012; Shpund et al., 2019). Iguchi, Matsui, et al. (2012) evaluated the simulated RSDs in a rainfall event during MC3E. The simulation well reproduced the RSD differences between deep convective clouds and shallow warm clouds, but large raindrops were simulated when the precipitation rate is small, which did not appear in the disdrometer observations. They speculated that the absence of spontaneous breakup in the bin microphysics scheme may have led to the preservation of large raindrops formed by the melting of ice particles. The aforementioned study of Shpund et al. (2019) also evaluated the simulated RSDs using disdrometer observations. Contrary to the simulated snow particle size distributions that showed some discrepancy with the aircraft observations, the simulated RSDs at the surface showed good agreement with the disdrometer observations. Chen et al. (2023) evaluated the performances of different cloud microphysics schemes (five bulk microphysics schemes and one bin microphysics scheme) in reproducing the observed RSD variability in an extreme rainfall event that occurred in Henan Province, China. In their results, the simulation with the bin microphysics scheme best reproduced the observed RSD variability although the simulated RSD variability was still not large enough.

The evaluation of RSDs simulated using bin microphysics schemes has been mostly based on a few RSD parameters that are thought to successfully represent the whole RSD characteristics (e.g., Chen et al., 2023; Iguchi, Matsui, et al., 2012). This approach is not different from what has been used to evaluate the RSDs simulated using bulk microphysics schemes (e.g., Jin & Baik, 2023; Lin et al., 2022; Wang et al., 2020). However, considering the bin microphysics schemes' capability of representing hydrometeor size distributions of various shapes, comparison of full RSDs between simulations and observations can provide additional valuable information. For example, the simulated RSDs may contain spurious peaks that do not appear in the observation (which will be shown in this study), or the multimodality of observed RSDs that appears under particular circumstances (Radhakrishna & Rao, 2009; Sauvageot & Koffi, 2000) may not be captured in simulations. Either of the abovementioned features can provide some insights into model deficiencies, but has not been investigated yet.

In this study, a precipitation event that occurred in South Korea during the passing of an extratropical cyclone is selected as a case for the evaluation of simulated RSDs. Cloud clusters accompanying an extratropical cyclone mostly consist of different types of clouds and precipitation (Field & Wodd, 2007; Houze, 2014), which can have significantly different cloud microphysics. As the RSDs at the surface reflect the microphysics in the clouds above, the RSDs during this event can substantially vary both spatially and temporally. Examining whether a bin microphysics scheme can reproduce the variation of RSD within this event is an interesting point of this study.

This study evaluates the detailed features of RSDs simulated using a bin microphysics scheme by comparing full RSDs with disdrometer observations for different sub-periods within a precipitation event associated with an extratropical cyclone. Then, we attempt to figure out the sources of biases in the bin microphysics scheme. In Section 2, the precipitation case, disdrometer data, and simulation setup are described. In Section 3, results and discussion are given. A summary and conclusions are provided in Section 4.

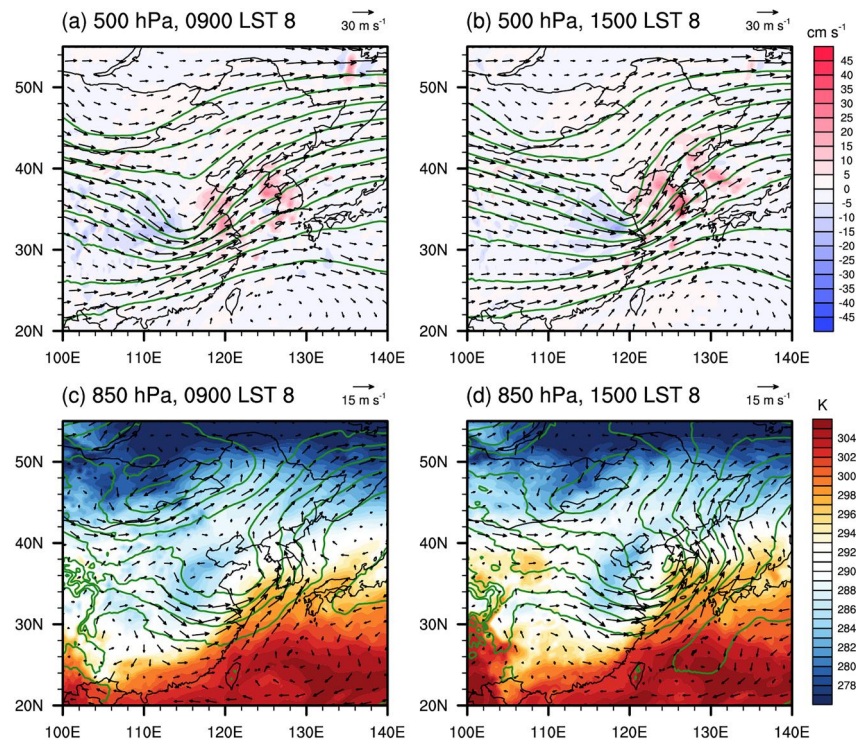


Figure 1. Fields of (a, b) 500-hPa and (c, d) 850-hPa geopotential height (green lines) and horizontal wind vectors (arrows) at (a, c) 0900 and (b, d) 1500 local standard time (LST) 8 November 2018. The color shades in (a) and (b) indicate the 500-hPa vertical velocity, and those in (c) and (d) indicate the 850-hPa equivalent potential temperature.

2. Data and Methods

2.1. Case Description

On 8 November 2018, an extratropical cyclone that developed over the East China Sea and moved northeast caused precipitation throughout South Korea. A large amount of precipitation occurred mainly in the north-western part of South Korea, and the 24-hr accumulated precipitation amount observed by a disdrometer in Seoul was 62 mm. Figure 1 shows the synoptic conditions for this precipitation event represented using the European Centre for Medium-Range Weather Forecasts reanalysis data (ERA5, Hersbach et al., 2020). At 0900 LST 8, a 500-hPa trough was located over eastern China and an 850-hPa trough was located to the east of the 500-hPa trough, indicating a westward tilt of the trough axis which is a favorable condition for a surface low-pressure system to develop. Along the east of the trough, updrafts occur at the 500-hPa level (Figure 1a). The low-level jet transports the warm and humid air toward South Korea (Figure 1c). At 1500 LST 8, the troughs at the 500-hPa and 850-hPa levels strengthen. The 500-hPa updrafts appear along the western coast of South Korea and become stronger than at 0900 LST 8 (Figure 1b). The transport of warm and humid air toward South Korea by the low-level jet is further intensified (Figure 1d).

2.2. Model Description and Simulation Setup

The Weather Research and Forecasting (WRF) model version 4.3.3 is used to simulate the precipitation event that occurred on 8 November 2018. The model domain configuration and the location of disdrometer are shown in Figure 2. Three one-way nested domains centered on South Korea are used. The numbers of horizontal and vertical grids for all three domains are

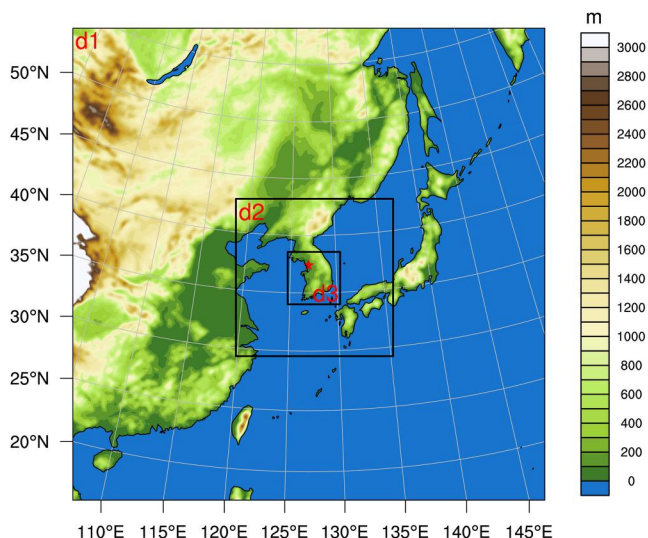


Figure 2. Model domain configuration with topography (shaded). The red star in domain 3 indicates the disdrometer site in Seoul.

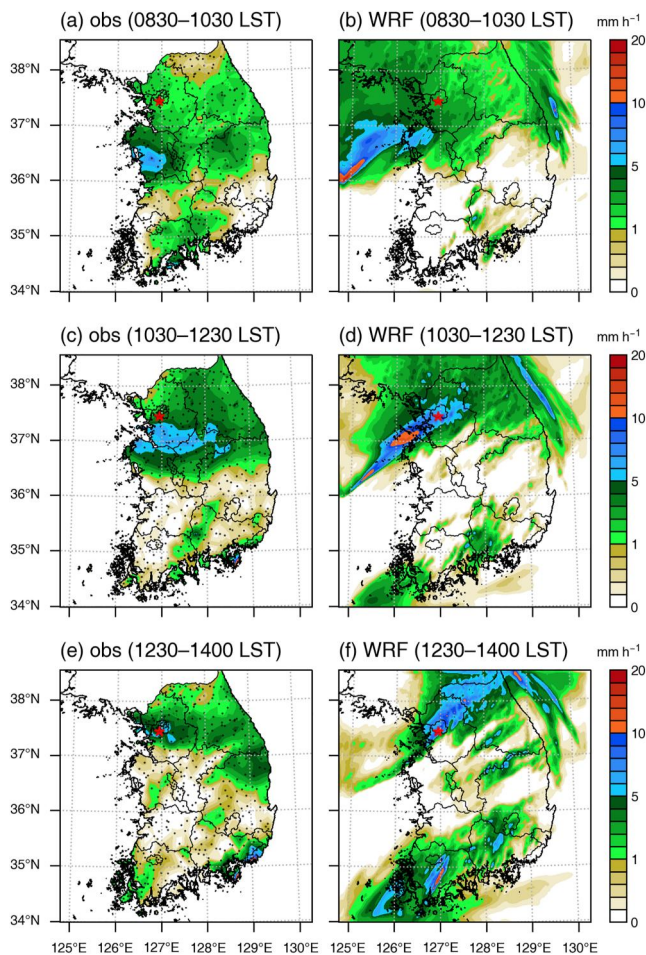


Figure 3. Spatial distributions of (a, c, e) observed and (b, d, f) simulated average rain rates for the periods of (a, b) 0830–1230 LST, (c, d) 1030–1230 LST, and (e, f) 1230–1400 LST. The black dots and red star represent the locations of rain gauges and disdrometer, respectively.

250 × 250 and 49, respectively. The horizontal grid spacings are 18, 6, and 2 km for domains 1, 2, and 3 respectively. The vertical grid is stretched from ~60 m for the lowest layer to ~450 m for the highest layer. The physical parameterizations considered in this simulation are the unified Noah land surface model (Tewari et al., 2004), the revised MM5 surface layer scheme (Jiménez et al., 2012), the University of Washington boundary layer scheme (Bretherton & Park, 2009), the Dudhia shortwave radiation (Dudhia, 1989), the Rapid Radiative Transfer Model (RRTM) longwave radiation scheme (Mlawer et al., 1997), the Kain–Fritsch cumulus parameterization scheme (Kain, 2004), and the modified version of bin cloud microphysics scheme in the Hebrew University Cloud Model (HUCM, Khain et al., 2011; Lee & Baik, 2016). Note that the cumulus parameterization scheme is used only for domains 1 and 2. The model is integrated for 18 hr starting from 2100 LST 7 November 2018, and the last 12 hr is used for analysis. As initial and boundary conditions, the ERA5 reanalysis data (Hersbach et al., 2020), which have a 1-hr temporal resolution and a 0.25° horizontal resolution, are used.

Unlike bulk microphysics schemes which parameterize the size distribution of any hydrometeor using some parameters, the modified version of bin microphysics scheme in the HUCM explicitly predicts the size distribution. In this scheme, 43 mass-doubling bins are considered for seven hydrometeor types (liquid drop, three types of ice crystal (column, plate, and dendrite), snow, graupel, and hail) and aerosol. The microphysical processes included are nucleation, vapor diffusion, collection, collisional breakup, sedimentation, freezing, melting, and secondary ice multiplication processes. For the collision process, turbulence-induced collision enhancement (Lee & Baik, 2016) is implemented in this version. Liquid water fractions of snow, graupel, and hail and rimed fraction of snow are predicted to calculate the time-dependent gradual melting and snow density and terminal velocity, respectively. In cloud microphysical analyses in Subsection 3.2, a size threshold that separates cloud droplets and raindrops is used (80 μm in diameter).

This bin scheme assumes an initial aerosol size distribution following the Twomey equation and Köhler equation and sets the aerosol number concentration to be constant up to an altitude of 2 km, beyond which it decreases with an e -folding depth of 2 km. The aerosol number concentration is

controlled by setting the number concentration of cloud condensation nuclei at 1% supersaturation (N_0). In this study, N_0 is set at a relatively low value of 300 cm⁻³, considering the clean environmental condition that exhibited relatively low particulate matter (PM) concentrations (5 and 9 μg m⁻³ for PM_{2.5} and PM₁₀, respectively) in this event in Seoul. The aerosols are removed through nucleation-scavenging and advection processes and replenished with a relaxation time of 1 hr following the aerosol replenishment scheme of Jiang and Wang (2014). More detailed information on the bin microphysics scheme can be found in Khain et al. (2011) and Lee and Baik (2016).

2.3. RSDs From the Disdrometer and the Bin Microphysics Scheme

For evaluation of RSDs simulated using a bin microphysics scheme, this study uses the data from Parsivel² disdrometer (Tokay et al., 2014) installed at Seoul National University in South Korea (37.45°N, 126.95°E; the red star in Figure 2). The observational site is situated on the rooftop of a building at an elevation of 142 m above mean sea level, and it is surrounded by a grassy area, free from neighboring structures. When precipitating particles pass through the laser sheet (180 mm long; 30 mm wide; 1 mm high) between the two heads of the disdrometer, the disdrometer optically measures the diameter and fall velocity of precipitating particles using the maximum attenuation of laser signal and the duration of precipitating particles within the laser sheet, respectively. The measured information about the diameter and fall velocity is assigned to the matrix of 32 size (0–26 mm) and 32 fall velocity (0–22.4 m s⁻¹) bins with a sampling interval of 1 min.

The number and resolution of size bins in the disdrometer data and the bin microphysics scheme are different. The disdrometer considers 32 non-uniform size bins and the bin microphysics scheme considers 43 mass-doubling size bins. For raindrops, the disdrometer uses the 3rd–23rd size bins (diameter range of 0.25–8 mm). First two size bins are not considered due to the low signal-to-noise ratio. To match as closely as possible with the diameter range of the disdrometer data, the 19th–33rd size bins (diameter range of 0.23–7.3 mm) of the bin microphysics scheme are used for RSD evaluation.

To remove erroneous data caused by measurement errors such as partial detection of drops at the edges of the laser sheet, splashing drops, drops affected by strong winds, and multiple small drops being perceived as one large drop, drops with fall velocities 60% larger or 60% smaller than theoretical values are excluded using the fall velocity–diameter relationship of Atlas et al. (1973). In addition, 1-min disdrometer data with the total drop count smaller than 100 or with the rain rate smaller than 0.05 mm hr^{−1} are excluded, and the remaining data are further refined by removing data where the duration of rainfall is less than 3 min (Thompson et al., 2015). To ensure a fair comparison between the simulated and observed RSDs, the abovementioned method of Thompson et al. (2015) is also applied to the simulated RSDs.

The RSDs from the disdrometer are obtained as follows:

$$N(D_i) = \sum_{j=1}^{32} \frac{n_{ij}}{A_i V_j \Delta t \Delta D_i}, \quad (1)$$

where D_i (mm) is the mid-value of the i th diameter bin, $N(D_i)$ (m^{−3} mm^{−1}) is the raindrop number per unit volume per unit size interval for the i th diameter bin, n_{ij} is the number of raindrops assigned to the i th diameter and j th fall velocity bin, A_i (m²) is the effective sampling area of the i th diameter bin, V_j (m s^{−1}) is the fall velocity of the j th fall velocity bin, Δt (s) is the sampling interval, and ΔD_i (mm) is the width of the i th diameter bin. The rain rate R (mm h^{−1}) is calculated as

$$R = 6\pi \times 10^{-4} \sum_{i=3}^{23} \sum_{j=1}^{32} D_i^3 \frac{n_{ij}}{A_i \Delta t}. \quad (2)$$

The rain rate in the simulation is calculated using the same method using the simulated RSDs and prescribed raindrop terminal velocity–diameter relationship in the bin microphysics scheme. Note that the simulated RSDs and RSD parameters are calculated at the lowest (~25 m above ground level) grid box which covers the location of the disdrometer site. As the grid size is 2 km × 2 km horizontally, the evaluation of simulated RSDs in comparison with a point observation may have some uncertainty arising from the small-scale spatial variability of RSDs (Raupach & Berne, 2016).

RSD parameters are calculated from both simulated and observed RSDs. The n th-order RSD moment M_n (m^{−3} mm ^{n}) is calculated by

$$M_n = \sum_{i=i_s}^{i_e} D_i^n N(D_i) \Delta D_i, \quad (3)$$

where (i_s, i_e) is (3, 23) for the disdrometer data and (19, 33) for the bin microphysics scheme. The mass-weighted mean diameter D_m (mm) and the generalized intercept parameter N_w (m^{−3} mm^{−1}) are calculated as follows:

$$D_m = \frac{M_4}{M_3}, \quad (4)$$

$$N_w = \frac{4^4}{\Gamma(4)} \left(\frac{M_3}{D_m^4} \right), \quad (5)$$

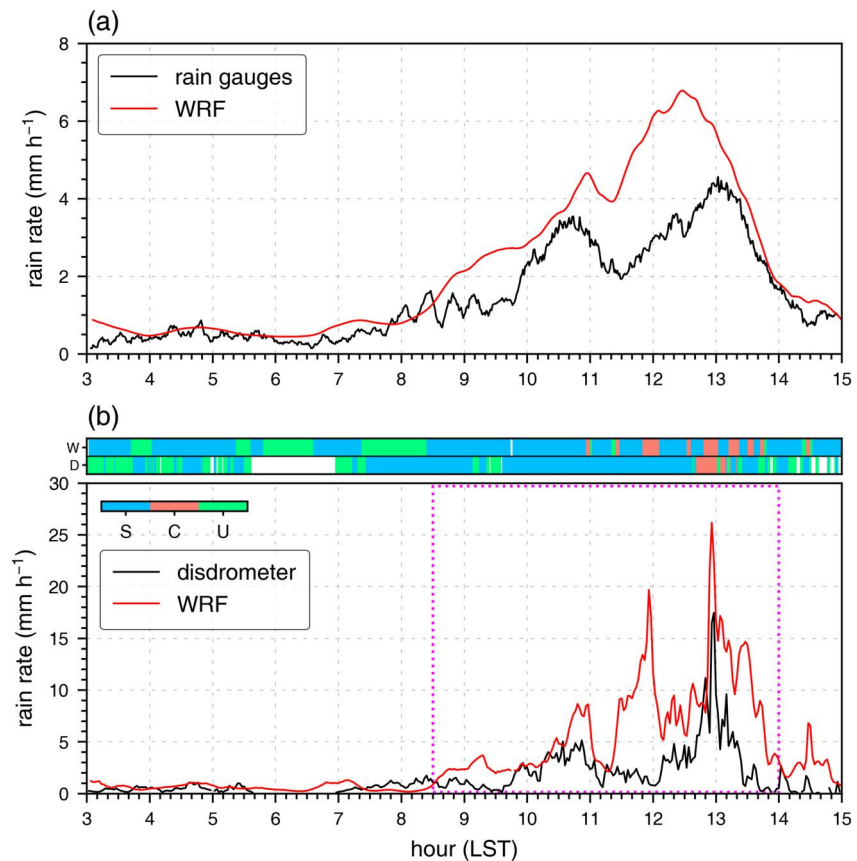


Figure 4. (a) Time series of rain rate in the rain gauge observation and simulation averaged over the locations of 110 rain gauges in the Seoul Metropolitan Area. (b) Time series of rain rate in the disdrometer observation and simulation at the disdrometer site. The rain type of each data in the WRF simulation (W) and disdrometer observation (D) is presented at the top of (b), which is categorized as stratiform (S), convective (C), and unclassified (U) following the method of Wen et al. (2016).

where Γ is the gamma function. The radar reflectivity factor Z (mm⁶ m⁻³) is defined by the sixth-order RSD moment. For comparison with the reflectivity observed from radar, Z is converted to the logarithmic scale in the unit of dBZ.

3. Results and Discussion

3.1. Evaluation of Simulated Raindrop Size Distributions

Figure 3 shows the spatial distributions of observed and simulated average rain rates for the periods of 0830–1030 LST, 1030–1230 LST, and 1230–1400 LST. The observation data are collected from 586 tipping bucket or weighing rain gauges operated by the Korea Meteorological Administration (KMA). For 0830–1030 LST, in both the observation and simulation, light rain is widespread over the northern part of South Korea and a rainband with moderate intensity approaches Seoul from its southwest (Figures 3a and 3b). For 1030–1230 LST, the approaching rainband in the observation is elongated in the west–east direction and is on the verge of entering Seoul, while the rainband in the simulation is elongated in the southwest–northeast direction and has already entered Seoul (Figures 3c and 3d). For 1230–1400 LST, Seoul is under the influence of the rainband with moderate or heavy intensity in both the observation and simulation (Figures 3e and 3f). Despite some differences in the orientation and moving speed of rainband, Seoul experiences the same rainband in both observation and simulation during this event.

Figure 4 shows the time series of rain rate averaged over the 110 rain gauges in the Seoul Metropolitan Area and the time series of the rain rate and rain type at the disdrometer site in the observation and the simulation. A 10-min

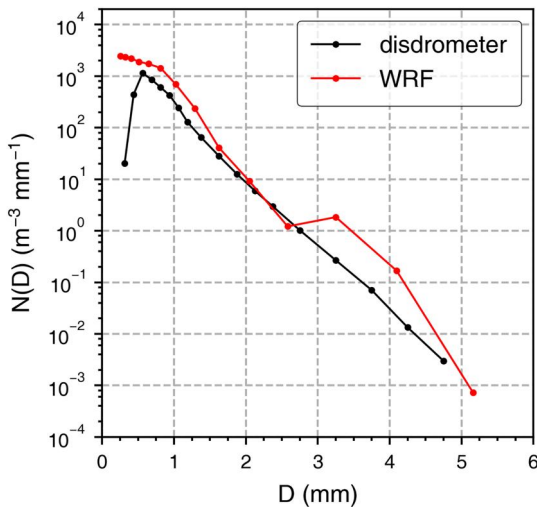


Figure 5. Simulated and observed raindrop size distributions at the disdrometer site averaged over the period of 0830–1400 LST.

moving average is applied to the times series. The rain type classification is done following the method of Wen et al. (2016). Rain is classified as stratiform if the rain rate is larger than 0.5 mm hr^{-1} and the 10-min standard deviation of rain rate is smaller than 1.5 mm hr^{-1} , and it is classified as convective if the rain rate is larger than 5 mm hr^{-1} and the 10-min standard deviation is larger than 1.5 mm hr^{-1} . Otherwise, it remains unclassified. In the Seoul Metropolitan Area (Figure 4a), the observed rain rate is small until ~ 0800 LST and increases to reach its first peak at 1044 LST, after which it decreases and increases again showing its highest peak at 1302 LST. The simulation overall well reproduces this trend of rain rate, with a slight delay of the first peak (1058 LST) and a slight advance of the highest peak (1228 LST). In the comparison between simulation and disdrometer observation (Figure 4b), moderate rain with weak temporal variability classified as stratiform rain during 0830–1030 LST and heavy rain with strong temporal variability classified as convective rain during 1230–1400 LST are well reproduced. It is noteworthy that the time of maximum rain rate in the simulation coincides with that in the observation (1256 LST), and rain at that time is classified as convective in both observation and simulation. The peak during 1120–1210 LST in the simulation is not seen in the observation, which is attributable to the slight mislocation of the simulated rainband. In the following analysis, the period of 0830–1400 LST is selected as a time window to evaluate the RSD prediction.

The simulated RSD averaged over the time window is compared to the disdrometer observation (Figure 5). For the comparison, the drop size bins from 0.256 to 6.502 mm in the simulation are used. The observed raindrop

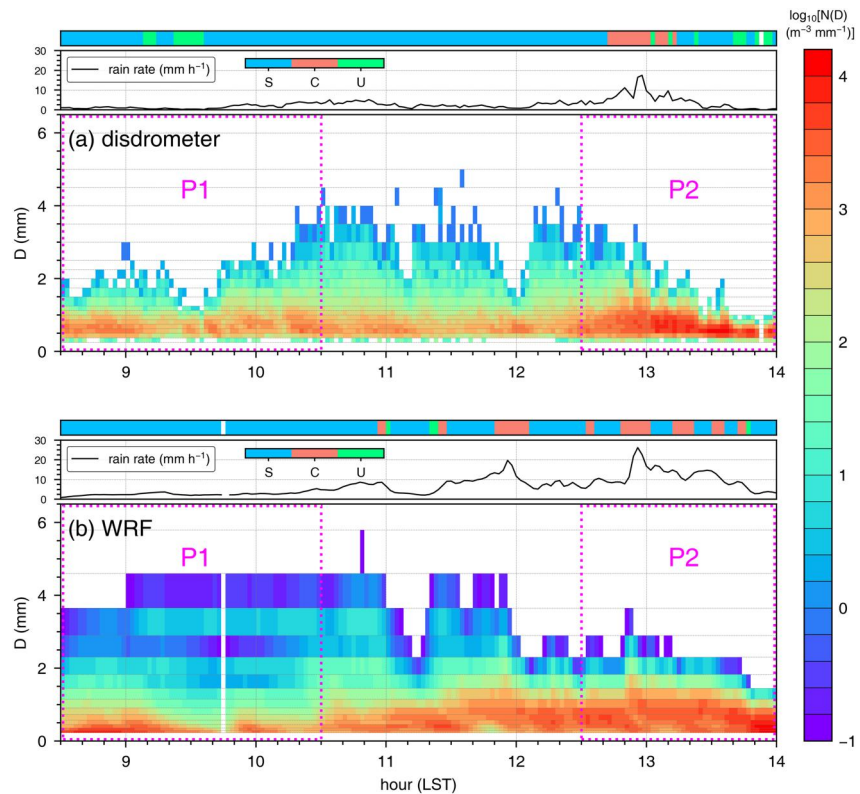


Figure 6. Time series of the logarithm of raindrop number concentration (shaded) in the (a) disdrometer observation and (b) simulation at the disdrometer site. The rain type of each data in the observation and simulation is presented at the top of each subfigure, which is categorized as stratiform (S), convective (C), and unclassified (U) following the method of Wen et al. (2016), along with the time series of rain rate.

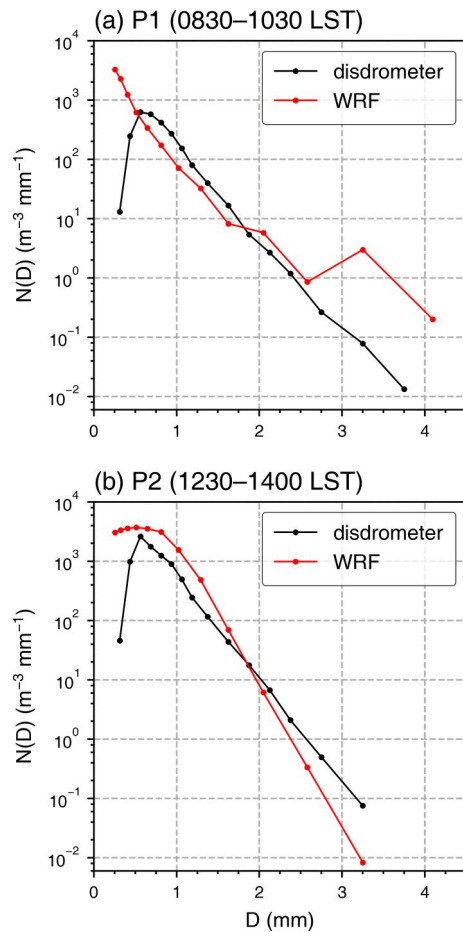


Figure 7. Simulated and observed raindrop size distributions at the disdrometer site in (a) Phase 1 (P1) and (b) Phase 2 (P2).

1030–1230 LST is excluded because of large discrepancies in rain rate and rain type between the observation and simulation (Figures 3c, 3d and 4b). The large discrepancies imply that the part of the precipitation system over the disdrometer site in this period is not properly reproduced in the simulation, which hinders a meaningful evaluation of the bin microphysics scheme's ability to predict RSDs. In the observation, P1 shows lower number concentration of small raindrops and a wider RSD than P2. The simulation captures these differences in RSD characteristics between P1 and P2, but the differences are somewhat exaggerated. In P1, the simulation overestimates the number concentration of large raindrops ($D > 3$ mm), showing a local maximum at $D = 3.3$ mm, and underestimates the number concentration of small raindrops ($D = 0.7$ – 1.6 mm) except for very small ones. In P2, the simulation overestimates the number concentration of small raindrops and underestimates the number concentration of intermediate and large raindrops. Among these biases, the overestimation of the number concentration of large raindrops in P1 and the overestimation of the number concentration of small raindrops in P2 are statistically significant at the 99% confidence level, and they are largely responsible for the two prominent biases in the mean RSD for the period of 0830–1400 LST shown in Figure 5.

The simulated and observed RSD characteristics in P1 and P2 are further compared using two widely used RSD parameters, the mass-weighted mean diameter D_m and the logarithm of generalized intercept parameter $\log_{10} N_w$. Figure 8 shows the scatter plots of simulated and observed D_m and $\log_{10} N_w$ with their means and temporal standard deviations for the whole time window, P1, and P2. For the whole time window, the simulation shows a larger mean value of D_m compared to the observation, while the mean value of $\log_{10} N_w$ is smaller than the observation. Note that when the small drop size range ($D < 0.56$ mm) which may be involved with measurement errors is excluded, the simulation–observation differences in mean D_m and $\log_{10} N_w$ are reduced by 26% and 33% in magnitudes, respectively, but their signs remain the same. Both the standard deviations of D_m and $\log_{10} N_w$ are

number concentration increases with diameter until its peak at 0.56 mm and then decreases monotonically. The simulation reproduces the overall decrease in $N(D)$ with diameter and particularly shows good agreement with the observation for the intermediate-diameter range. Meanwhile, there are some biases in the small- and large-diameter ranges. For small raindrops, $N(D)$ is overestimated by 1.4–2.4 times ($D = 0.56$ – 1.88 mm). Note that for further smaller drops ($D < 0.56$ mm), the observed $N(D)$ sharply decreases with decreasing diameter but this may be involved with systematic measurement errors (Park et al., 2017; Raupach et al., 2019; Thurai et al., 2017). For large raindrops, the simulation shows a local maximum of $N(D)$ at $D = 3.3$ mm while the observation does not. This results in an approximately one-order overestimation of $N(D)$ for $D = 3.3$ – 4.3 mm. The aforementioned overestimations of the number concentrations of small ($D = 0.56$ – 1.88 mm) and large ($D = 3.3$ – 4.3 mm) raindrops are both statistically significant at the 99% confidence level, where the statistical significance is obtained from Student's t -test, sampling 2-min interval observed and simulated RSDs.

For a more detailed evaluation, the time evolution of simulated RSD is compared to the observation (Figure 6). In the observation, during 0830–1230 LST when the stratiform rain is dominant, the RSDs are characterized by a relatively low number concentration of small raindrops and the presence of large raindrops ($D > 3.5$ mm), resulting in a relatively large variability of RSD spectrum width, compared to that during 1230–1400 LST. During 1230–1400 LST when the convective rain is largely involved, the RSDs are characterized by a high number concentration of small raindrops and the lack of large raindrops. This RSD evolution pattern is overall well captured in the simulation. However, a local maximum of $N(D)$ at $D = 3.3$ mm that is not seen in the observation persists in the stratiform rain until ~ 1200 LST, and the number concentration of small raindrops after 1230 LST is much larger than the observation.

These comparisons are clearly presented in Figure 7 that shows the observed and simulated average RSDs during two different time periods, Phase 1 (P1; 0830–1030 LST) and Phase 2 (P2; 1230–1400 LST). Here, the period during

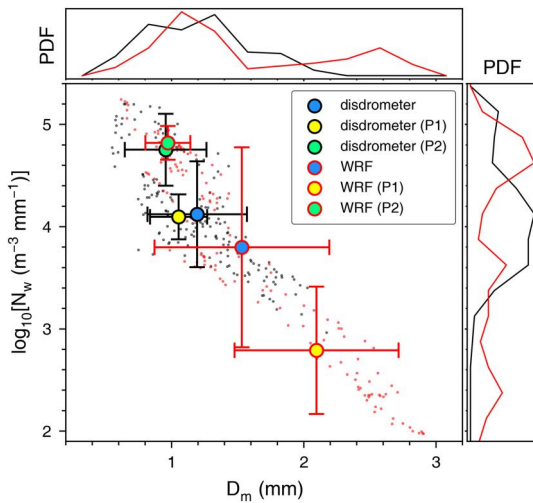


Figure 8. Mean values (filled circles) and ± 1 standard deviation (whiskers) of mass-weighted mean diameter D_m and the logarithm of generalized intercept parameter $\log_{10}N_w$ at the disdrometer site in the simulation and disdrometer observation. The blue, yellow, and green colors represent the whole time window (0830–1400 LST), P1 (0830–1030 LST), and P2 (1230–1400 LST). The probability density functions (PDFs) of D_m and $\log_{10}N_w$ are presented at the top and right side, respectively, where the red and black lines indicate the simulation and disdrometer observation, respectively.

larger in the simulation than in the observation. In the observation, P1 exhibits a larger mean D_m and a smaller mean $\log_{10}N_w$ than P2. The simulation also shows that P1 has a larger mean D_m and a smaller $\log_{10}N_w$ than P2, but the differences between P1 and P2 are much larger than in the observation. The large differences between P1 and P2 in the simulation are mainly attributed to the biases present in each phase. In P1, the simulation largely overestimates D_m by 1.0 mm and largely underestimates $\log_{10}N_w$ by 1.3, which is associated with the overestimation of the number concentration of large raindrops. In P2, D_m is similarly simulated, but $\log_{10}N_w$ is overestimated. This is associated with the overestimation of the number concentration of small raindrops. Consequently, the overestimated differences in D_m and $\log_{10}N_w$ between P1 and P2 results in the overly strong temporal variations of RSD in the simulation of this rain event. This is also indicated in the much wider PDFs of D_m and $\log_{10}N_w$. An interesting result is that in P2 when convective rain is largely involved, the standard deviations of D_m and $\log_{10}N_w$ in the simulation are rather smaller than those in the observation, as opposed to P1. This result agrees with that of Chen et al. (2023), who simulated a convective rainfall event and saw a lack of RSD variability in the simulation using a bin microphysics scheme compared to the observation.

The computation of the RSD parameters exhibits some dependence on the size bin spacings (Equations 3–5). Because the observed and simulated RSDs have different bin spacings, there can exist some uncertainty in the above comparison of D_m and $\log_{10}N_w$ (Figure 8) originating from the bin spacing difference. To examine whether the above comparison results are solid

regardless of the bin spacing difference, the uncertainty ranges of mean D_m and $\log_{10}N_w$ are estimated by considering two extreme assumptions, where the left and right boundary values of each diameter bin are respectively used to represent the diameter of the bin, instead of the mid-value. The uncertainty ranges of the simulated mean D_m and $\log_{10}N_w$ in the whole time window are 1.36–1.72 mm and 3.75–3.85, respectively, and do not overlap with those of the observed mean D_m (1.11–1.28 mm) and $\log_{10}N_w$ (4.10–4.14). This indicates that the overestimation of D_m and underestimation of $\log_{10}N_w$ are significant regardless of the bin spacing difference. Likewise, the overestimation (underestimation) of D_m ($\log_{10}N_w$) in P1 and the overestimation of $\log_{10}N_w$ in P2 described above are significant, with no overlaps of uncertainty ranges between the observation and simulation.

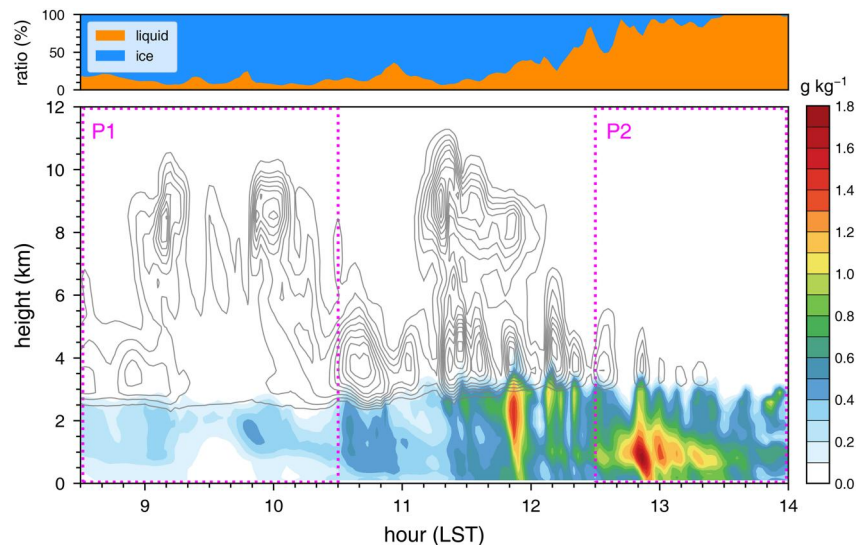


Figure 9. Time-height plot of mixing ratios of liquid-phase (shaded) and ice-phase (contoured) hydrometeors at the disdrometer site. The contours are in 0.3 g kg^{-1} intervals. At the top, the ratios of liquid and ice water paths to the total water path are presented.

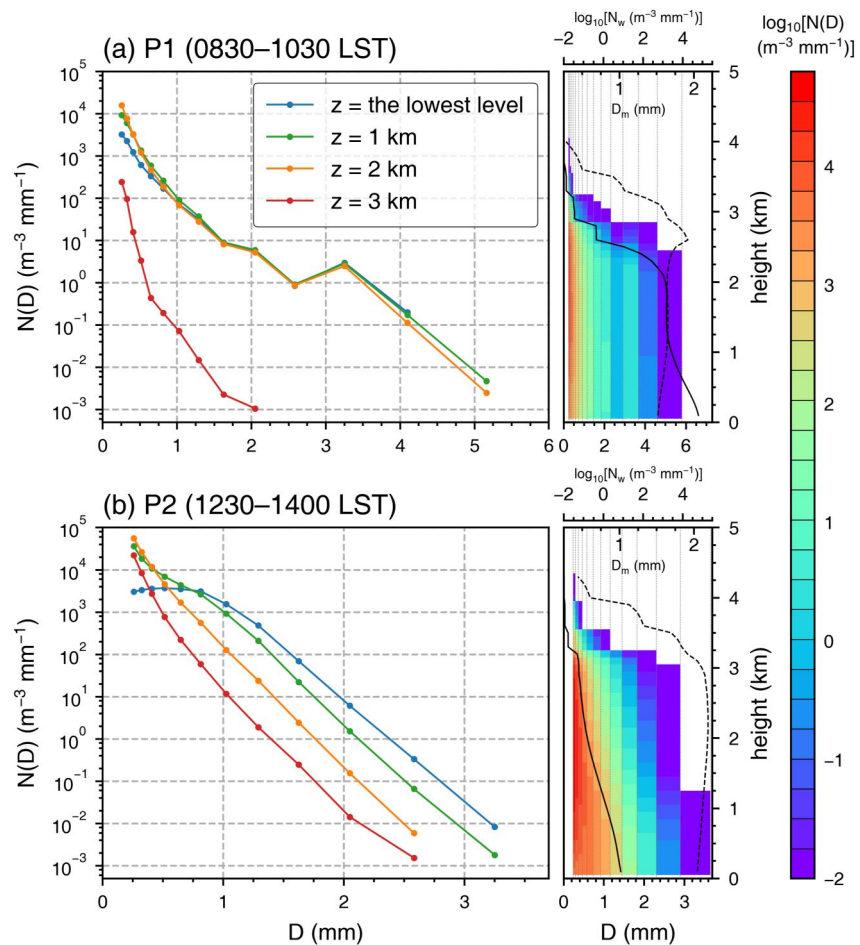


Figure 10. Simulated raindrop size distributions at different levels at the disdrometer site in (a) P1 and (b) P2. Vertical distributions of the logarithm of raindrop number concentration $\log_{10}N(D)$ (shaded), mass-weighted mean diameter D_m (solid line), and the logarithm of generalized intercept parameter $\log_{10}N_w$ (dashed line) are presented on the right side of each subfigure.

3.2. Possible Sources of the Biases in RSD Prediction

To examine the possible sources of the biases in RSD prediction shown in the previous subsection, it is necessary to understand the characteristics of the precipitation system and the cloud microphysics therein. Figure 9 shows the time-height plot of mixing ratios of liquid-phase and ice-phase hydrometeors and their ratio to the total mixing ratio. P1 and P2 are clearly distinguished by different cloud properties and microphysics. In P1, ice-phase hydrometeors are dominant, accounting for 87% of the total condensates on average. Consistent with the rain type classification which classifies the precipitation during P1 as stratiform rain, weak precipitation appears uniformly at altitudes below 2.5 km. In P2, clouds do not develop up to high altitudes and liquid-phase hydrometeor is predominant, accounting for 89% of the total condensates on average. Contrary to P1, the liquid water mixing ratio abruptly changes with time, resulting in a high temporal variability of rain rate and a much larger average rain rate in P2. Note that the time-averaged freezing level at the disdrometer site in P1 and P2 are 2.8 and 3.0 km, respectively.

Figure 10 shows the simulated RSDs at different levels in P1 and P2, along with the vertical distributions of RSD parameters. In P1, RSD undergoes an abrupt change from $z = 3$ km to $z = 2$ km, accompanied by a sharp increase in D_m from 0.4 to 1.6 mm. The RSD at $z = 2$ km exhibits a local maximum at $D = 3.3$ mm. The shape of RSD does not significantly change from this level to the surface, and particularly, the local maximum remains almost unchanged. Given that the existence of the local maximum at $D = 3.3$ mm in the simulation is a main discrepancy from the disdrometer observation in P1 (Figure 7a), the above result raises suspicions of an excessive production

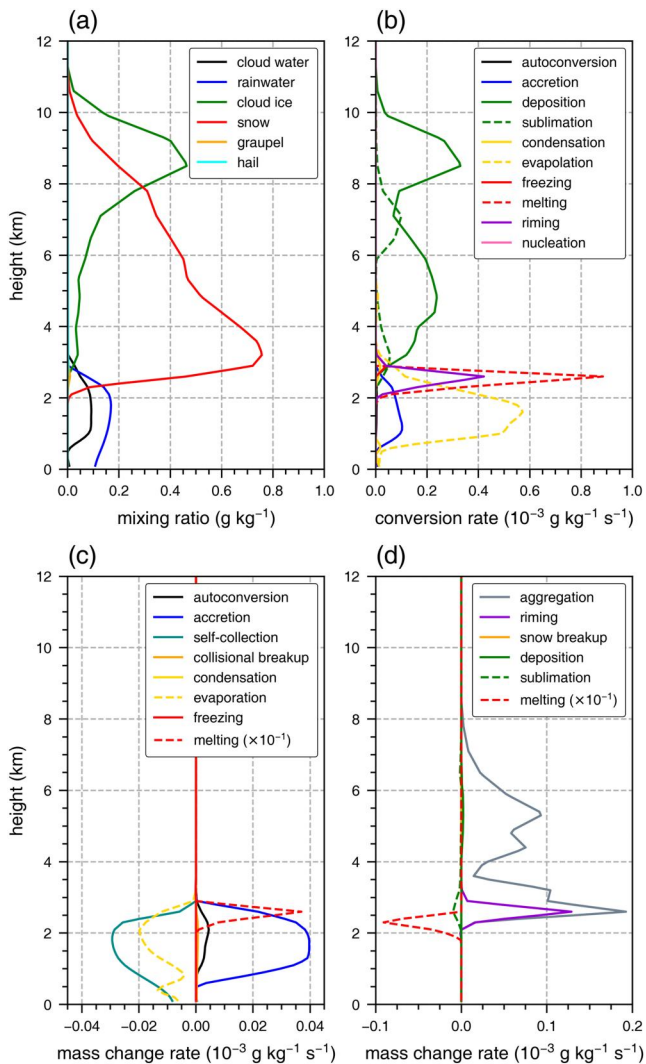


Figure 11. Vertical profiles of simulated (a) hydrometeor mixing ratios, (b) microphysical conversion rates, (c) microphysical mass change rates of raindrops of $D < 0.91$ mm, and (d) microphysical mass change rates of snow particles of $D_{eq} = 3.3$ mm at the disdrometer site in P1.

to reducing the number of small raindrops, but its contribution to the total mass of small raindrops is smaller than that of self-collection.

The above results suggest that the prominent bias in RSD prediction in P1, the existence of the local maximum at $D = 3.3$ mm, can be largely associated with snow melting. To further examine this association, the vertical evolution of simulated snow size distributions is presented in Figure 12. For a direct comparison with the RSD, the snow size distributions are presented as a function of equivalent melted diameter. The shape of snow size distribution at $z = 3$ km is very similar to the RSD at $z = 2$ km (Figure 10a). This confirms that the local maximum at $D = 3.3$ mm in RSD is produced by melting of snow, whose size distribution also exhibits the local maximum at the same equivalent melted diameter. The number concentration of snow particles at $D_{eq} = 3.3$ mm is gradually accumulated with decreasing height from $z = 9$ km to $z = 3$ km, and the local maximum is first formed at $z = 6$ km. At the altitudes where the local maximum is formed, no mixed-phase microphysical processes but only ice-phase microphysical processes take place (Figure 11b). The production of snow particles of $D_{eq} = 3.3$ mm at these altitudes is almost exclusively caused by aggregation, the collection process between ice particles (Figure 11d). Therefore, the local maximum in the snow size distributions is the result of active aggregation. This could be a source of RSD biases in P1 because the parameterization of ice–ice collection contains higher uncertainty than

of large raindrops at $z = 2$ – 3 km or insufficient depletion of those large raindrops during their falling, which will be examined further later in this subsection. Meanwhile, there do exist some minor changes in RSD from $z = 2$ km to the surface, which are the decrease in the number of very small raindrops and the slight increase in the number of intermediate and large raindrops. In contrast with P1, P2 shows gradual changes in RSD with decreasing height. The number concentration of very small raindrops decreases from $z = 2$ km with decreasing height, and the number concentration of intermediate and large raindrops significantly increases with decreasing height. Particularly, $N(D)$ for $D = 0.8$ – 2.6 mm increases by approximately two orders from $z = 3$ km to the lowest level. As a result, D_m gradually increases from $z = 3$ km to the lowest level and $\log_{10} N_w$ decreases a little below $z = 2$ km. However, the vertical changes in RSD seem to be not large enough, because the disdrometer observation exhibits even lower number concentration of small raindrops and even higher number concentration of large raindrops (Figure 7b).

Cloud microphysical processes in P1 and P2 are investigated separately to figure out the processes that act as the sources of the RSD biases in each phase. For P1, the vertical profiles of hydrometeor mixing ratios and microphysical process rates are presented in Figure 11. Clouds in P1 are characterized by a large amount of ice-phase hydrometeors, almost exclusively snow and cloud ice. Cloud ice prevails above $z \sim 8$ km, and snow is dominant from $z \sim 8$ km to $z \sim 2.5$ km with its peak located at $z = 3.2$ km. Cloud water and rainwater are rare above $z = 3.5$ km. The most prominent source of rainwater in P1 is melting, particularly melting of snow, actively occurring at $z \sim 2$ – 3 km. This suggests that the dramatic changes in RSD from $z = 3$ km to $z = 2$ km, that is, the appearance of the local maximum at $D = 3.3$ mm and the sharp increase in D_m (Figure 10a) are caused by melting of snow. Accretion of cloud water by rainwater is another source of rainwater in P1 that occurs within a wider vertical range ($z \sim 0.5$ – 3 km), but its contribution to the rainwater production is much smaller than that of melting. To RSDs in P1, the contribution of warm-rain collision–coalescence processes seems to be limited, which can be deduced from that the RSD does not significantly change from $z = 2$ km to the surface. Nevertheless, the decrease in the number of small raindrops and the slight increase in the number of large raindrops with decreasing height can be attributed to the warm-rain collision–coalescence processes, particularly the self-collection of raindrops (Figure 11c). Evaporation that is prominent below $z = 2.5$ km also contributes

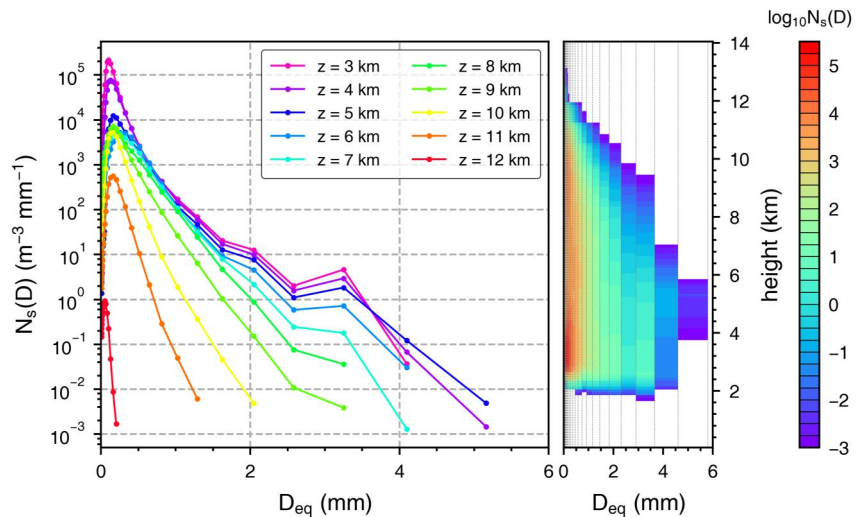


Figure 12. Simulated snow size distributions at different levels at the disdrometer site in P1. Vertical distribution of the logarithm of snow number concentration $\log_{10} N_s(D)$ (shaded) is presented on the right side.

that of ice–drop collection or drop–drop collection, due to the highly variable collection efficiency according to the ice particle shapes, temperature, and humidity (Khain et al., 2000) and the lack of observations to properly constrain it. The bin microphysics scheme used in this study employs temperature-dependent collection efficiency for ice–ice collection (Khain et al., 2011), but there still remains high uncertainty in the representation of collection efficiency. The analysis so far gives a conclusion that the overestimation of the number concentration of large raindrops at the surface in P1 may be originated from the overly active aggregation at upper levels.

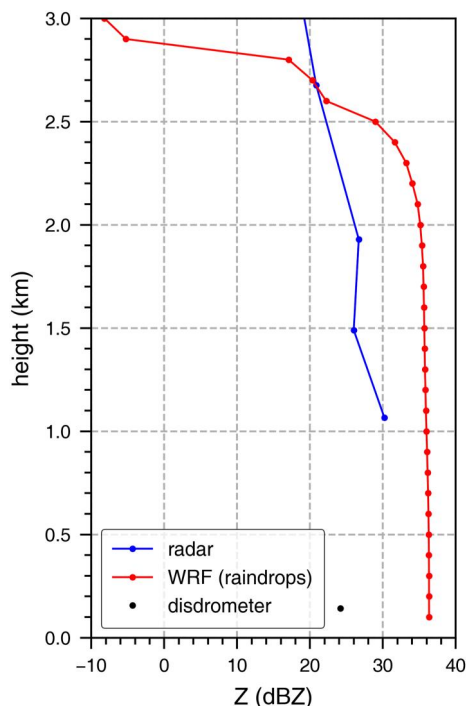


Figure 13. Vertical profiles of time-averaged radar reflectivity computed from the simulated RSDs at the disdrometer site in P1 in comparison with the radar and disdrometer observations. Note that the radar reflectivity in the simulation and disdrometer observation is computed from the RSDs only, while that in the radar observation includes signals from all condensates.

Besides the over-production of large raindrops, insufficient depletion of large raindrops during their falling could be another reason for the overestimation of large raindrops in P1. Large raindrops produced by melting of large snow particles can breakup into small drops either spontaneously or by collision with other drops. However, the number concentration of large raindrops in P1 rather keeps increasing with decreasing height below the melting layer (Figure 10a), which indicates that the number of large raindrops produced by collision–coalescence is larger than the number of those depleted by spontaneous or collisional breakup. Given that the disdrometer observation exhibits a lower number concentration of large raindrops and a higher number concentration of small raindrops ($D = 0.7$ – 1.6 mm) than the simulation in P1 (Figure 7a), the simulated RSD in P1 would be closer to the observed RSD if raindrop breakup were represented to be more active. Particularly, spontaneous breakup can be relatively more important than collisional breakup for large raindrops produced by melting (Paukert et al., 2019), but it is not considered in the bin microphysics scheme used in this study. Considering spontaneous breakup of raindrops in the bin microphysics scheme may contribute to reducing the RSD biases in P1.

Between the two suggested reasons for the overestimation of large raindrops in P1, the overly active aggregation is likely to be the primary reason. In Figure 13, the time-averaged radar reflectivity (in dBZ) computed from the simulated RSDs above the disdrometer site in P1 is compared to the radar and disdrometer observations. The radar data are obtained from an S-band (2,887 MHz) dual-polarization Doppler radar installed at Mt. Gwangdeok (38.12°N, 127.43°E), which is operated by KMA. At the surface, the

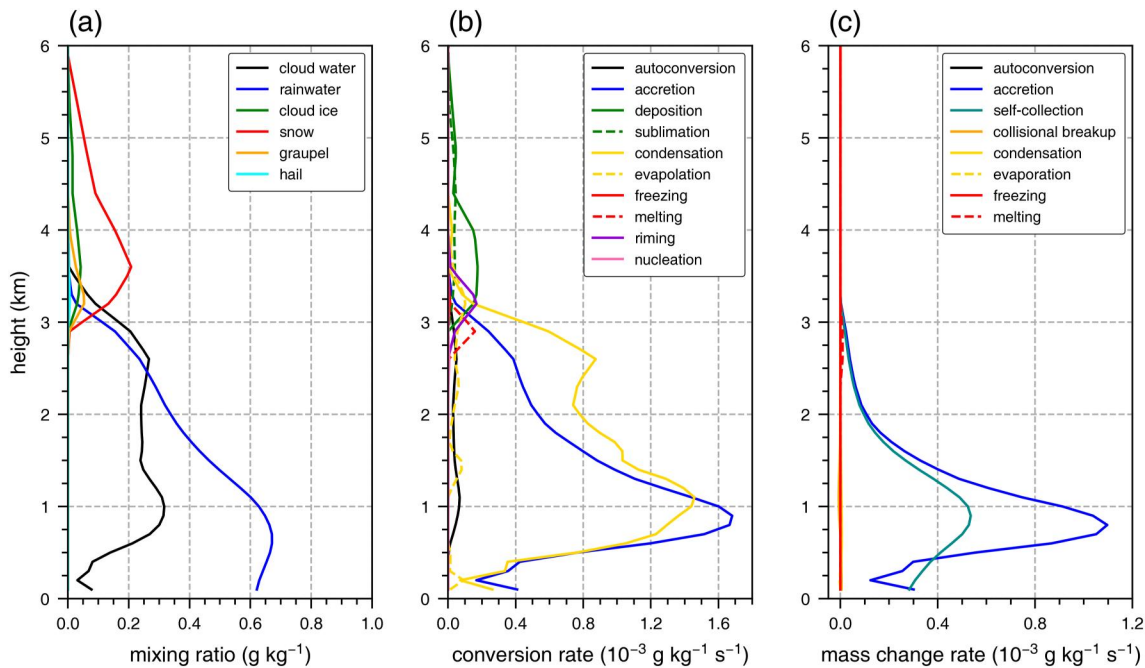


Figure 14. Vertical profiles of simulated (a) hydrometeor mixing ratios, (b) microphysical conversion rates, and (c) microphysical mass change rates of raindrops of $D > 0.91$ mm at the disdrometer site in P2. Note that the y-axis limit is different from that in Figure 11.

simulated radar reflectivity (36 dBZ) is much larger than the disdrometer observation (24 dBZ), representing the overestimation of large raindrops. Consistently, the overestimation of radar reflectivity also appears in comparison with the radar observation at altitudes above 1 km. It is notable that the overestimation of radar reflectivity is apparent at $z \sim 2$ km, the bottom of melting layer (35 dBZ compared to 26 dBZ). This indicates that this overestimation mainly originates from the melting of overly produced large snow particles (Figure 12) and that the consequent overestimation of large raindrops at this altitude predominantly causes the overestimation at the surface. From the bottom of melting layer to the surface, there is some degree of variation in the radar reflectivity bias and it may be associated with warm-rain processes such as raindrop breakup. However, it is relatively small compared to the pre-existing bias generated in the melting layer, which indicates that the warm-rain processes are not the primary reason for the overestimation of large raindrops at the surface.

Figure 14 shows the vertical profiles of hydrometeor mixing ratios and microphysical process rates in P2. In P2, liquid-phase hydrometeors (cloud water and rainwater) are dominant, and rainwater shows a bottom-heavy vertical profile with its peak at $z = 0.6$ km, indicating that rainwater is produced mainly by warm-rain processes. The mixing ratios of ice-phase hydrometeors are relatively small, and their melting does not significantly contribute to the rainwater production. In this phase, updraft takes place from near the surface to $z = 4$ km, with the peak at $z = 1.1$ km (not shown). As convective clouds are largely involved in this phase, vigorous condensation occurs and produces a large amount of liquid water mass. Raindrops are generated by autoconversion of cloud droplets that occurs throughout $z = 0.5$ –3 km and grow mainly by accretion of cloud droplets which is more active at lower levels. Active self-collection of raindrops continuously increases the number concentration of intermediate and large raindrops with decreasing height (Figure 10b) together with accretion of cloud droplets and also decreases the number concentration of small raindrops. Despite these vertical evolution of RSD via accretion and self-collection, the simulated number concentration of intermediate and large raindrops at the surface is still lower and that of small raindrops is still higher than the observation (Figure 7b). This implies that the collisional growth of raindrops in the simulation is weaker than that in reality.

Figure 15 shows the scatter plots of D_m and $\log_{10}N_w$ versus rain rate in the simulation and disdrometer observation in P2. D_m tends to increase as rain rate increases in both simulation and observation, indicating stronger collisional growth with increasing rain rate. However, for the whole range of rain rate, D_m of simulated RSD is relatively smaller than that of observed RSD at the same rain rate. Also, the simulation shows much larger

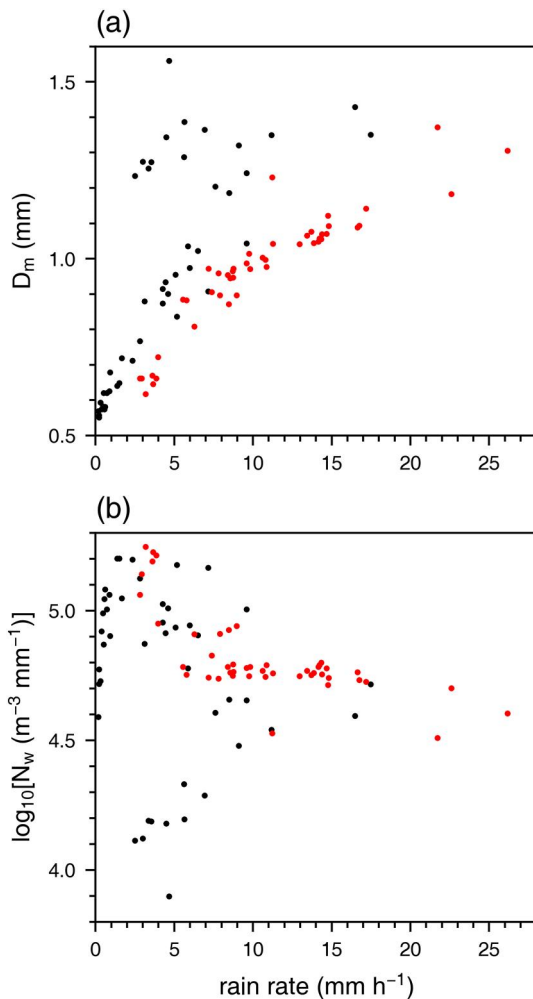


Figure 15. Scatter plots of (a) D_m and (b) $\log_{10}N_w$ versus rain rate at the disdrometer site in P2. Red and black dots indicate the simulation and disdrometer observation, respectively.

$\log_{10}N_w$ than the observation for the same rain rate. This shows that the insufficient collisional growth in the simulation is present regardless of the various rain rates in P2. The prescription of aerosol number concentration in the bin microphysics scheme used in this study can be one reason for the insufficient collisional growth of raindrops. The collisional growth of raindrops can be sensitive to the aerosol number concentration because it affects the number concentration of cloud droplets and thus all relevant microphysical processes (Chen et al., 2021; Fan et al., 2016; Lu & Seinfeld, 2006). A higher number concentration of cloud droplets with a given total mass indicates a smaller mean diameter of cloud droplets, which weakens auto-conversion of cloud droplets into raindrops. Accretional growth of raindrops, on the other hand, can become stronger as there remain more cloud droplets to collect. The changes in the warm-rain collision-coalescence processes can result in a change in RSD. To quantitatively examine the contribution of prescribed aerosol number concentration to the RSD biases, further investigation with additional numerical simulations using different prescribed aerosol number concentrations is needed.

4. Summary and Conclusions

In this study, we evaluated the raindrop size distributions simulated using a bin microphysics scheme through comparison with disdrometer observations, for a precipitation event associated with an extratropical cyclone passing South Korea. The mean RSD is overall well reproduced, but notable overestimations are seen in the small- and large-diameter ranges. The overestimation in large-diameter range is prominent in P1, when stratiform rain is predominant, and it is characterized by the appearance of a local maximum in RSD at $D = 3.3$ mm, which is not seen in the observed RSDs. This spurious local maximum originates from upper levels, where ice-ice collection generates a local maximum in snow size distribution, which is converted into that in RSD below the melting layer. Insufficient depletion of raindrops through breakup could be another reason for the overestimation of large raindrops in P1. The overestimation in small-diameter range is prominent in P2, when convective rain is largely involved. The warm-rain collision-coalescence is the largest contributor to RSDs in this period, but the RSD comparison shows that this process should have been represented to be stronger in the simulation.

Unlike bulk microphysics schemes that employ typical forms of particle size distributions that are obtained from observations, bin microphysics schemes allow any shape of distributions, which indicates that the particle size distributions in bin microphysics schemes are solely determined by physical processes. As a result, the issues in the representation of each physical process can be more apparently reflected in the simulated size distributions. This is exemplified by the spurious local maximum at $D = 3.3$ mm simulated in P1 that was found to be originated from the overly active ice-ice collection at upper levels. Consequently, evaluating simulated RSDs of a precipitation event can be an effective way of identifying deficiencies in the parameterizations of specific processes that significantly affect RSDs in the event. Considering together with different RSD characteristics depending on the type of precipitation system (Jwa et al., 2021; Loh et al., 2019), this suggests the need for similar investigations for other types of precipitation systems where other microphysical processes make significant contributions to RSDs.

Bin microphysics schemes have a significant advantage in calculating collection processes as they consider the collection efficiency that varies with the sizes of colliding particles and can accurately capture the evolution of particle size distribution resulting from collection. However, for reliable calculations, accurate collection efficiency data need to be provided, which are currently insufficient. To alleviate the biases in model prediction caused by uncertainties in collection efficiency, laboratory experiments and direct numerical simulations in diverse environmental conditions need to be conducted.

One limitation of this study is that the findings in this study are based on the results of a single simulation. Additional simulations with different initial aerosol concentrations or different dynamical realizations may enable the quantification of uncertainty in the RSD biases, but the high computational costs required by the bin microphysics scheme impose limitations in conducting additional simulations. For a clearer identification of systematic deficiencies of bin microphysics schemes, more studies on the observation-based evaluation of bin microphysics schemes are needed.

Data Availability Statement

The disdrometer data and WRF simulation outputs used in this study are given in Mendeley data (Lee, 2024). The rain gauge data and radar data provided by the Korea Meteorological Administration can be downloaded from <https://data.kma.go.kr>. The ERA5 reanalysis data provided by the Copernicus Climate Change Service (C3S) Climate Data Store (CDS, 2018b, 2018a) can be downloaded from <https://cds.climate.copernicus.eu/>.

Acknowledgments

We sincerely appreciate the comments of the two anonymous reviewers who provided constructive feedback, which significantly enhanced the quality of this article. This work was supported by the National Research Foundation of Korea under Grant 2021R1A2C1007044.

References

- Atlas, D., Srivastava, R. C., & Sekhon, R. S. (1973). Doppler radar characteristics of precipitation at vertical incidence. *Reviews of Geophysics and Space Physics*, 11, 1–35. <https://doi.org/10.1029/rg011i001p00001>
- Bretherton, C. S., & Park, S. (2009). A new moist turbulence parameterization in the Community Atmosphere Model. *Journal of Climate*, 22(12), 3422–3448. <https://doi.org/10.1175/2008jcli2556.1>
- CDS. (2018a). ERA5 hourly data on pressure levels from 1940 to present. [Dataset]. *Copernicus Climate Change Service (C3S) Climate Data Store (CDS)*. Retrieved from <https://cds.climate.copernicus.eu/cdsapp#!/dataset/reanalysis-era5-pressure-levels?tab=overview>
- CDS. (2018b). ERA5 hourly data on single levels from 1940 to present. [Dataset]. *Copernicus Climate Change Service (C3S) Climate Data Store (CDS)*. Retrieved from <https://cds.climate.copernicus.eu/portfolio/dataset/reanalysis-era5-single-levels>
- Chen, G., Lu, Y., Hua, S., Liu, Q., Zhao, K., Zheng, Y., et al. (2023). Evaluating the variability of simulated raindrop size distributions in the “21-7” Henan extremely heavy rainfall event. *Geophysical Research Letters*, 50(8), e2023GL102849. <https://doi.org/10.1029/2023gl102849>
- Chen, Y.-C., Wang, S.-H., Min, Q., Lu, S., Lin, P.-L., Lin, N.-H., et al. (2021). Aerosol impacts on warm-cloud microphysics and drizzle in a moderately polluted environment. *Atmospheric Chemistry and Physics*, 21(6), 4487–4502. <https://doi.org/10.5194/acp-21-4487-2021>
- Dudhia, J. (1989). Numerical study of convection observed during the Winter Monsoon Experiment using a mesoscale two-dimensional model. *Journal of the Atmospheric Sciences*, 46(20), 3077–3107. [https://doi.org/10.1175/1520-0469\(1989\)046<3077:nsocod>2.0.co;2](https://doi.org/10.1175/1520-0469(1989)046<3077:nsocod>2.0.co;2)
- Fan, J., Wang, Y., Rosenfeld, D., & Liu, X. (2016). Review of aerosol–cloud interactions: Mechanisms, significance, and challenges. *Journal of the Atmospheric Sciences*, 73(11), 4221–4252. <https://doi.org/10.1175/jas-d-16-0037.1>
- Field, P. R., & Wadd, R. (2007). Precipitation and cloud structure in midlatitude cyclones. *Journal of Climate*, 20(2), 233–254. <https://doi.org/10.1175/jcli3998.1>
- Fridlind, A. M., Li, X., Wu, D., van Lier-Walqui, M., Ackerman, A. S., Tao, W.-K., et al. (2017). Derivation of aerosol profiles for MC3E convection studies and use in simulations of the 20 May squall line case. *Atmospheric Chemistry and Physics*, 17(9), 5947–5972. <https://doi.org/10.5194/acp-17-5947-2017>
- Grabowski, W. W., Morrison, H., Shima, S.-I., Abade, G. C., Dziekan, P., & Pawlowska, H. (2019). Modeling of cloud microphysics: Can we do better? *Bulletin of the American Meteorological Society*, 100(4), 655–672. <https://doi.org/10.1175/bams-d-18-0005.1>
- Hernández Pardo, L., Machado, L. A. T., Morrison, H., Cecchini, M. A., Andreae, M. O., Pöhlker, C., et al. (2021). Observed and simulated variability of droplet spectral dispersion in convective clouds over the Amazon. *Journal of Geophysical Research: Atmospheres*, 126(20), e2021JD035076. <https://doi.org/10.1029/2021jd035076>
- Hersbach, H., Bell, B., Berrisford, P., Hirahara, S., Horányi, A., Muñoz-Sabater, J., et al. (2020). The ERA5 global reanalysis. *Quarterly Journal of the Royal Meteorological Society*, 146(730), 1999–2049. <https://doi.org/10.1002/qj.3803>
- Houze, R. A., Jr. (2014). *Cloud dynamics* (2nd ed.). Academic Press.
- Iguchi, T., Matsui, T., Tokay, A., Kollias, P., & Tao, W.-K. (2012). Two distinct modes in one-day rainfall event during MC3E field campaign: Analyses of disdrometer observations and WRF-SBM simulation. *Geophysical Research Letters*, 39(24), L24805. <https://doi.org/10.1029/2012gl053329>
- Iguchi, T., Nakajima, T., Khain, A. P., Saito, K., Takemura, T., Okamoto, H., et al. (2012). Evaluation of cloud microphysics in JMA-NHM simulations using bin or bulk microphysical schemes through comparison with cloud radar observations. *Journal of the Atmospheric Sciences*, 69(8), 2566–2586. <https://doi.org/10.1175/jas-d-11-0213.1>
- Jiang, Q., & Wang, S. (2014). Aerosol replenishment and cloud morphology: A VOCALS example. *Journal of the Atmospheric Sciences*, 71(1), 300–311. <https://doi.org/10.1175/jas-d-13-0128.1>
- Jiménez, P. A., Dudhia, J., González-Rouco, J. F., Navarro, J., Montávez, J. P., & García-Bustamante, E. (2012). A revised scheme for the WRF surface layer formulation. *Monthly Weather Review*, 140(3), 898–918. <https://doi.org/10.1175/mwr-d-11-00056.1>
- Jin, H.-G., & Baik, J.-J. (2023). Do double-moment microphysics schemes make reliable predictions on the raindrop number concentration? A squall-line case study. *Journal of Geophysical Research: Atmospheres*, 128(9), e2022JD038394. <https://doi.org/10.1029/2022jd038394>
- Jwa, M., Jin, H.-G., Lee, J., Moon, S., & Baik, J.-J. (2021). Characteristics of raindrop size distribution in Seoul, South Korea according to rain and weather types. *Asia-Pacific Journal of Atmospheric Sciences*, 57(3), 605–617. <https://doi.org/10.1007/s13143-020-00219-w>
- Kain, J. S. (2004). The Kain–Fritsch convective parameterization: An update. *Journal of Applied Meteorology*, 43(1), 170–181. [https://doi.org/10.1175/1520-0450\(2004\)043<0170:tkcpau>2.0.co;2](https://doi.org/10.1175/1520-0450(2004)043<0170:tkcpau>2.0.co;2)
- Khain, A., Ovtchinnikov, M., Pinsky, M., Pokrovsky, A., & Krugliak, H. (2000). Notes on the state-of-the-art numerical modeling of cloud microphysics. *Atmospheric Research*, 55(3–4), 159–224. [https://doi.org/10.1016/s0169-8095\(00\)00064-8](https://doi.org/10.1016/s0169-8095(00)00064-8)
- Khain, A., Rosenfeld, D., Pokrovsky, A., Blahak, U., & Ryzhkov, A. (2011). The role of CCN in precipitation and hail in a mid-latitude storm as seen in simulations using a spectral (bin) microphysics model in a 2D dynamic frame. *Atmospheric Research*, 99(1), 129–146. <https://doi.org/10.1016/j.atmosres.2010.09.015>

- Khairoutdinov, M. F., & Kogan, Y. L. (1999). A large eddy simulation model with explicit microphysics: Validation against aircraft observations of a stratocumulus-topped boundary layer. *Journal of the Atmospheric Sciences*, 56(13), 2115–2131. [https://doi.org/10.1175/1520-0469\(1999\)056<2115:alesmw>2.0.co;2](https://doi.org/10.1175/1520-0469(1999)056<2115:alesmw>2.0.co;2)
- Lee, H., & Baik, J.-J. (2016). Effects of turbulence-induced collision enhancement on heavy precipitation: The 21 September 2010 case over the Korean Peninsula. *Journal of Geophysical Research: Atmospheres*, 121(20), 12319–12342. <https://doi.org/10.1002/2016jd025168>
- Lee, H., & Baik, J.-J. (2018). A comparative study of bin and bulk cloud microphysics schemes in simulating a heavy precipitation case. *Atmosphere*, 9(12), 475. <https://doi.org/10.3390/atmos9120475>
- Lee, J. (2024). Data for “Raindrop Size Distributions Simulated Using a Bin Microphysics Scheme: Different Biases in Stratiform and Convective Rain from an Extratropical Cyclone” (Version 2). [Dataset]. *Mendeley Data*. <https://doi.org/10.17632/g6b4stc97s.2>
- Lin, L., Yuan, H., Bao, X., Chen, W., Zhang, S., & Xu, F. (2022). Evaluation of the raindrop size distribution representation of microphysics schemes in Typhoon Lekima using disdrometer network observations. *Atmospheric Research*, 278, 106346. <https://doi.org/10.1016/j.atmosres.2022.106346>
- Loh, J. L., Lee, D.-I., & You, C.-H. (2019). Inter-comparison of DSDs between Jincheon and Miryang at South Korea. *Atmospheric Research*, 227, 52–65. <https://doi.org/10.1016/j.atmosres.2019.04.031>
- Lu, M.-L., & Seinfeld, J. H. (2006). Effect of aerosol number concentration on cloud droplet dispersion: A large-eddy simulation study and implications for aerosol indirect forcing. *Journal of Geophysical Research: Atmospheres*, 111(D2), D02207. <https://doi.org/10.1029/2005jd006419>
- Lynn, B., & Khain, A. (2007). Utilization of spectral bin microphysics and bulk parameterization schemes to simulate the cloud structure and precipitation in a mesoscale rain event. *Journal of Geophysical Research: Atmospheres*, 112(D22), D22205. <https://doi.org/10.1029/2007jd008475>
- Mlawer, E. J., Taubman, S. J., Brown, P. D., Iacono, M. J., & Clough, S. A. (1997). Radiative transfer for inhomogeneous atmospheres: RRTM, a validated correlated-k model for the longwave. *Journal of Geophysical Research*, 102(D14), 16663–16682. <https://doi.org/10.1029/97jd00237>
- Morrison, H., Lawson, P., & Chandrakar, K. K. (2022). Observed and bin model simulated evolution of drop size distributions in high-based cumulus congestus over the United Arab Emirates. *Journal of Geophysical Research: Atmospheres*, 127(3), e2021JD035711. <https://doi.org/10.1029/2021jd035711>
- Morrison, H., Witte, M., Bryan, G. H., Harrington, J. Y., & Lebo, Z. J. (2018). Broadening of modeled cloud droplet spectra using bin microphysics in an Eulerian spatial domain. *Journal of the Atmospheric Sciences*, 75(11), 4005–4030. <https://doi.org/10.1175/jas-d-18-0055.1>
- Park, S.-G., Kim, H.-L., Ham, Y.-W., & Jung, S.-H. (2017). Comparative evaluation of the OTT PARSIVEL² using a collocated two-dimensional video disdrometer. *Journal of Atmospheric and Oceanic Technology*, 34(9), 2059–2082. <https://doi.org/10.1175/jtech-d-16-0256.1>
- Paukert, M., Fan, J., Rasch, P. J., Morrison, H., Milbrandt, J. A., Shpund, J., & Khain, A. (2019). Three-moment representation of rain in a bulk microphysics model. *Journal of Advances in Modeling Earth Systems*, 11(1), 257–277. <https://doi.org/10.1029/2018ms001512>
- Radhakrishna, B., & Rao, T. N. (2009). Multipeak raindrop size distribution observed by UHF/VHF wind profilers during the passage of a mesoscale convective system. *Monthly Weather Review*, 137(3), 976–990. <https://doi.org/10.1175/2008mwr2607.1>
- Raupach, T. H., & Berne, A. (2016). Small-scale variability of the raindrop size distribution and its effect on areal rainfall retrieval. *Journal of Hydrometeorology*, 17(7), 2077–2104. <https://doi.org/10.1175/jhm-d-15-0214.1>
- Raupach, T. H., Thurai, M., Bringi, V. N., & Berne, A. (2019). Reconstructing the drizzle mode of the raindrop size distribution using double-moment normalization. *Journal of Applied Meteorology and Climatology*, 58(1), 145–164. <https://doi.org/10.1175/jamc-d-18-0156.1>
- Rosenfeld, D., & Ulbrich, C. W. (2003). *Cloud microphysical properties, processes, and rainfall estimation opportunities*. In R. M. Wakimoto & R. C. Srivastava (Eds.), *Radar and atmospheric science: A collection of essays in honor of David Atlas, Meteorological Monographs* (Vol. 30, pp. 237–258). American Meteorological Society.
- Sauvageot, H., & Koffi, M. (2000). Multimodal raindrop size distributions. *Journal of the Atmospheric Sciences*, 57(15), 2480–2492. [https://doi.org/10.1175/1520-0469\(2000\)057<2480:mrsd>2.0.co;2](https://doi.org/10.1175/1520-0469(2000)057<2480:mrsd>2.0.co;2)
- Shpund, J., Khain, A., Lynn, B., Fan, J., Han, B., Ryzhkov, A., et al. (2019). Simulating a mesoscale convective system using WRF with a new spectral bin microphysics: 1: Hail vs graupel. *Journal of Geophysical Research: Atmospheres*, 124(24), 14072–14101. <https://doi.org/10.1029/2019jd030576>
- Tewari, M., Chen, F., Wang, W., Dudhia, J., LeMone, M. A., Mitchell, K., et al. (2004). *Implementation and verification of the unified Noah land surface model in the WRF model*. In *Paper Presented at 20th Conference on Weather Analysis and Forecasting/16th Conference on Numerical Weather Prediction*. American Meteorological Society.
- Thompson, E. J., Rutledge, S. A., Dolan, B., & Thurai, M. (2015). Drop size distributions and radar observations of convective and stratiform rain over the equatorial Indian and west Pacific Oceans. *Journal of the Atmospheric Sciences*, 72(11), 4091–4125. <https://doi.org/10.1175/jas-d-14-0206.1>
- Thurai, M., Gatlin, P., Bringi, V. N., Petersen, W., Kennedy, P., Notaroš, B., & Carey, L. (2017). Toward completing the raindrop size spectrum: Case studies involving 2D-video disdrometer, droplet spectrometer, and polarimetric radar measurements. *Journal of Applied Meteorology and Climatology*, 56(4), 877–896. <https://doi.org/10.1175/jamc-d-16-0304.1>
- Tokay, A., Wolff, D. B., & Petersen, W. A. (2014). Evaluation of the new version of the laser-optical disdrometer, OTT Parsivel². *Journal of Atmospheric and Oceanic Technology*, 31(6), 1276–1288. <https://doi.org/10.1175/jtech-d-13-00174.1>
- Wang, M., Zhao, K., Pan, Y., & Xue, M. (2020). Evaluation of simulated drop size distributions and microphysical processes using polarimetric radar observations for landfalling Typhoon Matmo (2014). *Journal of Geophysical Research: Atmospheres*, 125(6), e2019JD031527. <https://doi.org/10.1029/2019jd031527>
- Wen, L., Zhao, K., Zhang, G., Xue, M., Zhou, B., Liu, S., & Chen, X. (2016). Statistical characteristics of raindrop size distributions observed in East China during the Asian summer monsoon season using 2-D video disdrometer and Micro Rain Radar data. *Journal of Geophysical Research: Atmospheres*, 121(5), 2265–2282. <https://doi.org/10.1002/2015jd024160>
- Witte, M. K., Chuang, P. Y., Ayala, O., Wang, L.-P., & Feingold, G. (2019). Comparison of observed and simulated drop size distributions from large-eddy simulations with bin microphysics. *Monthly Weather Review*, 147(2), 477–493. <https://doi.org/10.1175/mwr-d-18-0242.1>